Arecibo-green bank-LOFAR carbon radio recombination line observations toward cold H I clouds

Roshi, D.A.; Peters, W.M.; Emig, K.L.; Salas, P.; Oonk, J.B.R.; Lebrón, M.E.; Dickey, J.M.

Arecibo-Green Bank-LOFAR Carbon Radio Recombination Line Observations toward Cold H I Clouds

D. Anish Roshi[1,2] , W. M. Peters[3] , K. L. Emig[4,11] , P. Salas[5] , J. B. R. Oonk[6,7,8] , M. E. Lebrón[9] , and J. M. Dickey[10]

[1] Arecibo Observatory, Road 625 Final, Bo Esperanza, Arecibo, PR 00612, USA
[2] University of Central Florida, 4000 Central Florida Boulevard, Orlando, FL 32816, USA
[3] Naval Research Laboratory, Washington, DC, USA
[4] National Radio Astronomy Observatory, 520 Edgemont Road, Charlottesville, VA 22903, USA
[5] Green Bank Observatory, 155 Observatory Road, Green Bank, WV 24915, USA
[6] Leiden Observatory, Leiden University, P.O. Box 9513, NL-2300 RA Leiden, The Netherlands
[7] Netherlands Institute for Radio Astronomy (ASTRON), Postbus 2, 7990 AA Dwingeloo, The Netherlands
[8] SURF/SURFsara, Science Park 140, 1098 XG Amsterdam, The Netherlands
[9] Department of Physical Sciences, University of Puerto Rico, Río Piedras Campus, San Juan, PR 00931, USA
[10] School of Natural Sciences, University of Tasmania, Hobart, TAS 7001, Australia

Abstract

We present results from a search for radio recombination lines in three H I self-absorbing (HISA) clouds at 750 MHz and 321 MHz with the Robert C. Byrd Green Bank Telescope, and in three Galactic plane positions at 327 MHz with the Arecibo Telescope. We detect carbon recombination lines (CRRLs) in the direction of DR4 and DR21, as well as in the Galactic plane position G34.94 + 0.0. We additionally detect hydrogen recombination lines in emission in five of the six sightlines, and a Helium line at 750 MHz toward DR21. Combining our new data with 150 MHz Low Frequency Array detections of CRRL absorption toward DR4 and DR21, we estimate the electron densities of the line-forming regions by modeling the line width as a function of frequency. The estimated densities are in the range $1.4 \rightarrow 6.5$ cm^{-3} toward DR4, for electron temperatures $200 \rightarrow 20$ K. A dual line-forming region with densities between $3.5 \rightarrow 24$ cm^{-3} and $0.008 \rightarrow 0.3$ cm^{-3} could plausibly explain the observed line width as a function of frequency on the DR21 sight line. The central velocities of the CRRLs compare well with CO emission and HISA lines in these directions. The cloud densities estimated from the CO lines are smaller (at least a factor of five) than those of the CRRL-forming regions. It is likely that the CRRL-forming and HISA gas is located in a denser, shocked region either at the boundary of or within the CO emitting cloud.

1. Introduction

Stars form from the collapse of molecular clouds, which must, in turn, be formed continuously in order to sustain star formation in the Galaxy. It has been suggested that a fraction of the interstellar regions exhibiting H I self-absorption (HISA) are sites of molecular cloud formation (Gibson et al. 2000; Klaassen et al. 2005). HISA occurs when foreground cold atomic gas absorbs the 21 cm emission line from warm H I gas behind it. Many HISA regions have a low atomic fraction but little or no ^{12}CO emission, implying that a significant amount of "CO dark" molecular gas is present (Klaassen et al. 2005). In other cases the HISA is well mixed with CO emitting molecular gas (Li & Goldsmith 2003).

While spectral line studies have inferred molecular gas content in HISA regions, observational constraints on the molecular formation process are still lacking. There are a few possible molecular formation processes that have been discussed in the literature (see review by Dobbs et al. 2014). These include a converging flow, such as a gas flow caused by the expansion of an H II region or supernova remnant (SNR), which could enhance the local gas density resulting in the formation of molecules. Another possibility is a quasi-static cloud contraction process where a slight increase in ambient pressure accelerates the phase transition from atomic to molecular gas.

Observations of radio recombination lines (RRLs) of ionized carbon, H I 21 cm absorption, and CO emission may be used to put constraints on the molecular formation processes in HISA regions. RRL optical depth has a strong inverse dependence on the electron temperature ($\propto T_e^{-2.5}$, where T_e is the electron temperature). Thus RRLs from ionized carbon (CRRLs) are preferentially detected toward cold regions. The inferred neutral gas densities toward HISA regions are a few times 10^3 cm^{-3} (Li & Goldsmith 2003; Klaassen et al. 2005). CRRLs from neutral regions with such densities are expected to be brighter at lower frequencies ($\lesssim 1$ GHz; Kantharia & Anantharamaiah 2001; Roshi & Kantharia 2011; Salgado et al. 2017a).

The detection of low-frequency CRRLs from a well-known HISA region—the Heeschen-Riegel-Crutcher region (HRC; Heeschen 1955; Riegel & Crutcher 1972)—was reported by Roshi & Kantharia (2011) and Oonk et al. (2019). By combining multifrequency CRRL and H I data, Roshi & Kantharia (2011) were able to constrain the physical properties and processes in the HRC cloud. These include electron temperature, electron density, line-of-sight (LOS) path length, hydrogen nuclear density, hydrogen atomic density, and hydrogen molecular density. The derived physical properties along with constraints on the background ultraviolet (UV) radiation field were then used to estimate the H$_2$ formation and dissociation rates in the cloud. They show that the H$_2$ formation rate exceeds the H$_2$ dissociation rate, suggesting that the cloud is in the process of converting H I

Table 1
Summary of Observations

Source Name	R.A. (2000) (hh:mm:ss)	Decl. (2000) (dd:mm:ss)	Date of Obs. yyyy-mm-dd		Obs. Freq (MHz)	Beam (°)	Telescope
DR4 (G78.12+1.92)	20:21:56	+40:15:36		2012-05-09	321,750	0.66, 0.3	GBT
DR21 (G81.68+0.54)	20:39:01	+42:19:43	2012-05-09,	2012-05-27	321,750	0.66, 0.3	GBT
HB21 (G89.00+4.70)	20:46:05	+50:39:05		2012-05-09	750	0.66	GBT
G34.20 + 0.0	18:53:45.1	+01:07:43	2019-06-03,	2020-05-11	327	0.25	Arecibo
G34.94 + 0.0	18:55:06.1	+01:47:14	2019-06-02,	2020-05-08	327	0.25	Arecibo
			2020-06-01,	2020-06-02			
G35.17 + 0.0	18:55:31.3	+01:59:30	2019-05-27,	2020-04-26	327	0.25	Arecibo

to H_2 and will convert all of its atomic hydrogen into the molecular form over a timescale $\gtrsim 10^5$ years.

In this paper, we expand our observational study toward the HISA regions detected along the sightlines toward the H II region DR21, and the SNRs DR4 & HB21. These were selected based on HISA detection in the Leiden/Argentine/Bonn 21 cm line survey data (Kalberla et al. 2005). Unlike the HRC cloud, the selected directions have intense background far-UV radiation fields due to the presence of star-forming regions. These observations therefore will allow us to probe molecular formation in very different environments compared to the HRC cloud. RRL observations were made with the Robert C. Byrd Green Bank Telescope (GBT) at 321 and 750 MHz. We also present results from blind recombination line observations made toward three positions (G34.20+0.0, G34.94+0.0, G35.17 +0.0) in the Galactic plane with the Arecibo telescope. These observations were made at 327 MHz. The positions were selected because an earlier CRRL survey has detected lines in this part of the Galactic plane with an angular resolution of $2° \times 0°.5$ (Roshi et al. 2002). The observations and data analysis procedure are described in Sections 2 and 3, respectively. The results of recombination line observations and the estimation of physical properties by combining our data with LOw Frequency ARray (LOFAR; van Haarlem et al. 2013) and other previous CRRL observations (J. B. R. Oonk et al. 2021, in preparation) and existing H I and CO line data are presented in Section 4. A summary of the results and future work are given in Section 5.

2. Observations

The source name, coordinates, date of observations, center frequency of observations, FWHM beamwidth, and the telescope used for the observations are given in Table 1.

The 321 and 750 MHz observations with the GBT (project code GBT12A-352) used the Green Bank Spectrometer for measuring the power spectrum. For the 750 MHz observations, the spectrometer was configured to have eight 12.5 MHz sub-bands, with each sub-band divided into 4096 spectral channels. The sub-bands were tuned to observe eight α RRL transitions ($n = 201$, 203, 205 to 210, $\Delta n = 1$) within the PF1_800 receiver bandwidth. We use the quantum number $n = 206$ when referring to the final spectrum at this frequency obtained by averaging all of the transitions (see Section 3; also Table 2). The RRL transitions were selected such that they are located at frequency ranges relatively free of strong radio frequency interference (RFI). We observed in "standard frequency switch" mode, with a switching period of 1 s and frequency offset of 2.0 MHz ($\sim$815 km s^{-1} at the observing frequency).

For the 321 MHz observations, we used three 12.5 MHz sub-bands with 8192 spectral channels each to observe RRLs with the

PF1_342 receiver. The three sub-bands were centered at the observing frequencies 325.15, 309.62, and 341.87 MHz. The separation between RRL transitions near 340 MHz is $\sim$3.7 MHz. Thus multiple RRL transitions were observed in each sub-band. The RRLs observed are the α-transitions corresponding to $n = 268$, 271, 273, 275, 276, and 277. We use the quantum number $n = 273$ when referring to the final spectrum at this frequency obtained by averaging all of the transitions (see Section 3; also Table 2). We observed in "standard frequency switch" mode, with a switching period of 1 s and frequency offset of 1.0 MHz ($\sim$910 km s^{-1}). We used nine-level sampling mode since observations were to be made in the presence of RFI; although, these transitions were relatively free of strong RFI. We observed 3C 295 to determine the telescope pointing correction and for flux density calibration.

We used the Mock spectrometer for the 327 MHz Arecibo observations (Project code A3333). The 327 MHz receiver has a 3 dB bandwidth of $\sim$30 MHz, and there are eight α RRL transitions (principal quantum number $n = 268$ to 275, $\Delta n = 1$) within this frequency range. We configured the Mock spectrometer with a 160 MHz clock frequency and set the bandwidth divisor to four to observe all eight RRL transitions simultaneously. This configuration provided 40 MHz observing bandwidth with 8192 spectral channels, for a spectral resolution of 4.9 kHz. The observations were made in a "pseudo" frequency switching mode based on the standing waves in the blocked aperture of the telescope, which have a separation in frequency of $\sim$1.1 MHz. Each one minute scan in "standard on" mode was followed by scans offset by -500 and $+500$ km s^{-1} from the source velocity. At the central rest frequency of 326.5 MHz, this corresponds to switching the first local oscillator frequency by $\sim$545 kHz. The ± 500 km s^{-1} shift allowed us to observe all eight hydrogen and carbon RRLs simultaneously, because they are separated by only 149.6 km s^{-1}. The power spectrum was integrated for 1 s, and 60 of them were written to a fits file every minute at the end of each scan. We observed a "standard ON/OFF" scan with calibrated noise switching at the beginning of each observation to measure the on-source continuum antenna temperature. We also observed a flux density calibrator, 3C 394, in "standard ON/OFF" mode with noise switching to calibrate the noise cal value in janskys.

3. Data Reduction

We used GBTIDL[12,13] to create 1 s integration bandpass-corrected spectra for the GBT observations. GBTIDL routines were also used to correct the bandpass for each sub-band from the frequency switched data set. The GBTIDL routine vshift

---

[12] https://gbtidl.nrao.edu/
[13] https://www.l3harrisgeospatial.com/Software-Technology/IDL

Table 2
Observed RRL Parameters

Freq. (MHz)	Atom	n	T_{LA} (K)	V_{LSR} (km s^{-1})	ΔV (km s^{-1})	Note
			DR4 (G78.12+1.92)			
321	H	273	0.77(0.05)	1.4(0.8)	26.5(1.9)	
	C		0.77(0.09)	−2.8(0.4)	6.6(0.9)	
750	H	206	0.46(0.01)	0.9(0.2)	25.0(0.5)	
	C		0.24(0.02)	−2.6(0.2)	5.1(0.5)	
150	C	350	−4.2(0.1)	−1.7(0.1)	$\Delta V_L = 7.4(0.9)$	1
	C		−3.8(0.1)	−1.8(0.1)	$\Delta V_L = 8.5(1.0)$	2
	C		−4.3(0.2)	−1.7(0.2)	$\Delta V_L = 7.5(1.3)$	3
	C		−3.8(0.1)	−1.8(0.2)	$\Delta V_L = 7.3(1.2)$	4
			DR21 (G81.68+0.54)			
321	H	273	0.76(0.03)	7.2(0.5)	28.1(1.3)	
	C		0.63(0.05)	8.8(0.4)	7.0(0.9)	
	C		0.22(0.05)	−2.1(1.3)	9.3(3.2)	
750	H	206	0.66(0.01)	6.9(0.1)	25.3(0.2)	
	He		0.05(0.01)	7.8(1.0)	16.2(2.4)	
	C		0.21(0.01)	−2.1(0.1)	4.1(0.3)	
	C		0.11(0.01)	8.6(0.3)	7.4(0.8)	
			0.09(0.02)	−2.9(0.2)	2.4(0.5)	10
150	C	350	−1.1(0.1)	−2.0(0.3)	$\Delta V_L = 17.1(2.1)$	5
	C		−1.1(0.1)	−1.6(0.3)	$\Delta V_L = 17.2(1.9)$	6
	C		−1.1(0.1)	−2.3(0.3)	$\Delta V_L = 10.2(2.3)$	7
	C		−1.0(0.1)	−1.9(0.3)	$\Delta V_L = 10.6(2.2)$	8
			HB21 (G89.00+4.70)			
750		206	(0.005)			
			G34.20 + 0.0			
327	H	272	0.26(0.03)	62.8(3.6)	58.6(8.6)	9
	C		0.25(0.06)	49.8(2.1)	11.0(4.9)	9
			G34.94 + 0.0			
327	H	272	0.43(0.04)	52.1(1.6)	32.7(3.7)	
	C		0.24(0.05)	49.4(2.2)	18.5(5.1)	
			G35.17 + 0.0			
327	H	272	0.15(0.01)	56.9(2.7)	48.5(6.4)	9

Notes.
[1] Parameters obtained from the spectrum averaged over 0°.3. A third-order polynomial baseline was removed from the spectrum. $\Delta V_D = 5.1$ km s^{-1}.
[2] Parameters obtained from the spectrum averaged over 0°.66. A third-order polynomial baseline was removed from the spectrum. $\Delta V_D = 5.1$ km s^{-1}.
[3] Parameters obtained from the spectrum averaged over 0°.3. $\Delta V_D = 5.1$ km s^{-1}.
[4] Parameters obtained from the spectrum averaged over 0°.66. $\Delta V_D = 5.1$ km s^{-1}.
[5] Parameters obtained from the spectrum averaged over 0°.3. A third-order polynomial baseline was removed from the spectrum. $\Delta V_D = 4.1$ km s^{-1}.
[6] Parameters obtained from the spectrum averaged over 0°.66. A third-order polynomial baseline was removed from the spectrum. $\Delta V_D = 4.1$ km s^{-1}.
[7] Parameters obtained from the spectrum averaged over 0°.3. $\Delta V_D = 4.1$ km s^{-1}.
[8] Parameters obtained from the spectrum averaged over 0°.66. $\Delta V_D = 4.1$ km s^{-1}.
[9] Tentative detection.
[10] See Section 4.2.

was used to apply local standard of rest (LSR) velocity correction for each CRRL transition. The bandpass- and velocity-corrected spectra were written to a text file for each CRRL transition. These spectra were then edited for RFI.

The RFI affected data may be sorted into three types: (a) A majority (90%) of the RFI were narrow band, confined to one or two spectral channels. The amplitude of each varies slowly over several tens of minutes. (b) In a few cases (40% of the observing time), the frequency and strength of the RFI were time dependent, but could be easily identified in 1 s integrated spectra. (c) Rarely (10% of the observing time), the frequency of RFI sweeps across a large fraction of the sub-bands in a few seconds. Excising the RFI thus requires careful editing of the data both in time and frequency domains, for which we developed an RFI-editing program in MATLAB.[14]

The RFI-editing program uses a channel weighting scheme to edit out the RFI. Each channel is assigned unity weight at the start. If a channel is identified as affected by RFI or corrupted

by instrumental problems, then the weight of that channel is set to zero. The weighted spectra are then averaged across time. Identification of RFI is currently done manually by examining each 1 s spectrum. For the GBT data sets, the weighted average spectrum forms the final spectrum for each RRL transition and sight line.

We followed similar steps to analyze the Arecibo data set. Phil Perillat's IDL routines[15] were used to generate a spectrum covering the full 40 MHz bandwidth. A spectrum covering a 1000 km s^{-1} range centered on each of the eight RRL transitions was extracted. These spectra were then edited for RFI using the MATLAB RFI-editing routine described above, and the weighted average was taken to get the spectrum corresponding to each RRL transition. Because the observations were made with in-band frequency switching, each RRL spectrum was "folded" to improve the integration time. The spectra were re-sampled using a Fourier transform method (Roshi et al. 2005) and aligned in velocity range. The "folded" spectra for the different transitions were then re-sampled to a common velocity resolution and averaged to get the final integrated spectrum. This analysis method was tested by observing an off-source position for 2 hr with the Arecibo telescope at 327 MHz. No spurious line-like feature was detected in this data setup to a 50 mK level. The weights were processed in the same way as the spectrum during the resampling process, so the final spectrum has associated channel weights. These indicate the number of 1 s data points included in each spectral channel. Figure 1 shows an example RRL spectrum toward G34.94 + 0.0 obtained with the Arecibo telescope along with the weights. The typical variation in weights across the final averaged spectrum is ∼10%.

4. Results

The observed positions are shown in Figure 2 (see Table 1). The RRL spectra obtained toward these positions are shown in Figures 3 and 4. The frequency of observation, atom producing the RRL, line antenna temperature, LSR velocity, and FWHM line width obtained from the spectra are given in Table 2. CRRLs were detected toward DR4, DR21, G34.94 + 0.0, and G34.2 + 0.0 (tentative detection) at all of the observed frequencies. Hydrogen lines were detected toward positions DR4, DR21, G34.90 + 0.0, G34.2 + 0.0 (tentative detection), and G35.17 + 0.0 (tentative detection) at all of the observed frequencies. Helium and heavy-element recombination lines were detected toward DR21 at 750 MHz. No lines were detected toward HB21, with a limiting sensitivity of 5 mK. The listed line widths are corrected for broadening due to spectral resolution using the equation $\sqrt{\Delta V_{\rm obs}^2 - \Delta V_{\rm res}^2}$, where $\Delta V_{\rm obs}$ is the observed line width, and $\Delta V_{\rm res}$ is the spectral resolution.

In the following subsections we combine our new RRL observations with LOFAR and other existing CRRL, H I, and CO data sets to constrain the physical properties of the line-forming regions. The implicit simplifying assumptions made in the modeling presented below to estimate the physical properties are that the line-forming region is homogeneous gas with uniform temperature and density. A brief discussion of the observed hydrogen and helium line formation is also presented. We note here that the LOFAR detections of CRRLs in absorption near 150 MHz toward DR4 (see Section 4.1.2)
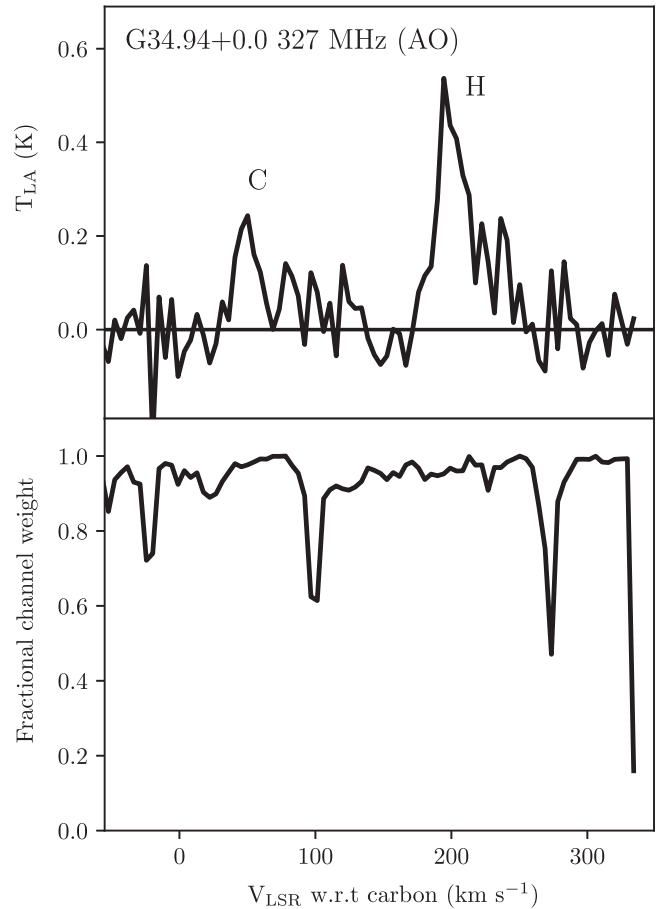

Figure 1. Recombination line spectrum along with the fractional channel weights. The weighted averaged spectrum toward G34.94 + 0.0 obtained with the Arecibo telescope at 327 MHz is shown in the top plot, and the fractional channel weights are shown in the bottom plot. The typical variation in weights across channels in the final averaged spectrum is about 10%.

and DR21 (see Section 4.2.1) are the highest-frequency carbon recombination line absorption reported to date.

4.1. DR4

DR4 is a shell-type SNR located in the Cygnus X region. A detailed study of the H I 21 cm line associated with the SNR was done by Landecker et al. (1980) and Ladouceur & Pineault (2008). They used data from the Dominion Radio Astrophysical Observatory synthesis telescope; Ladouceur & Pineault (2008) also used the CGPS data set (Taylor et al. 2003). The angular resolution of the 21 cm observations was better than 2.′5. The H I line emission and absorption in this direction are quite complex. The 21 cm line analysis indicates that the SNR blast wave is compressing the H I gas into a shell. The velocity structure of the H I line could be explained as an expanding shell (either due to the SNR blast or the stellar wind of the progenitor) with speed ∼25 km s^{-1}. The near-side of the shell is seen in H I absorption against the bright SNR and also against the 21 cm emission from the far-side part of the shell (i.e., as HISA).

4.1.1. Cold Gas Properties Derived Using 21 cm Line Data

The CGPS H I spectra averaged over an area that matches the GBT beam of 0.66° at 321 MHz and 0.°3 at 750 MHz are
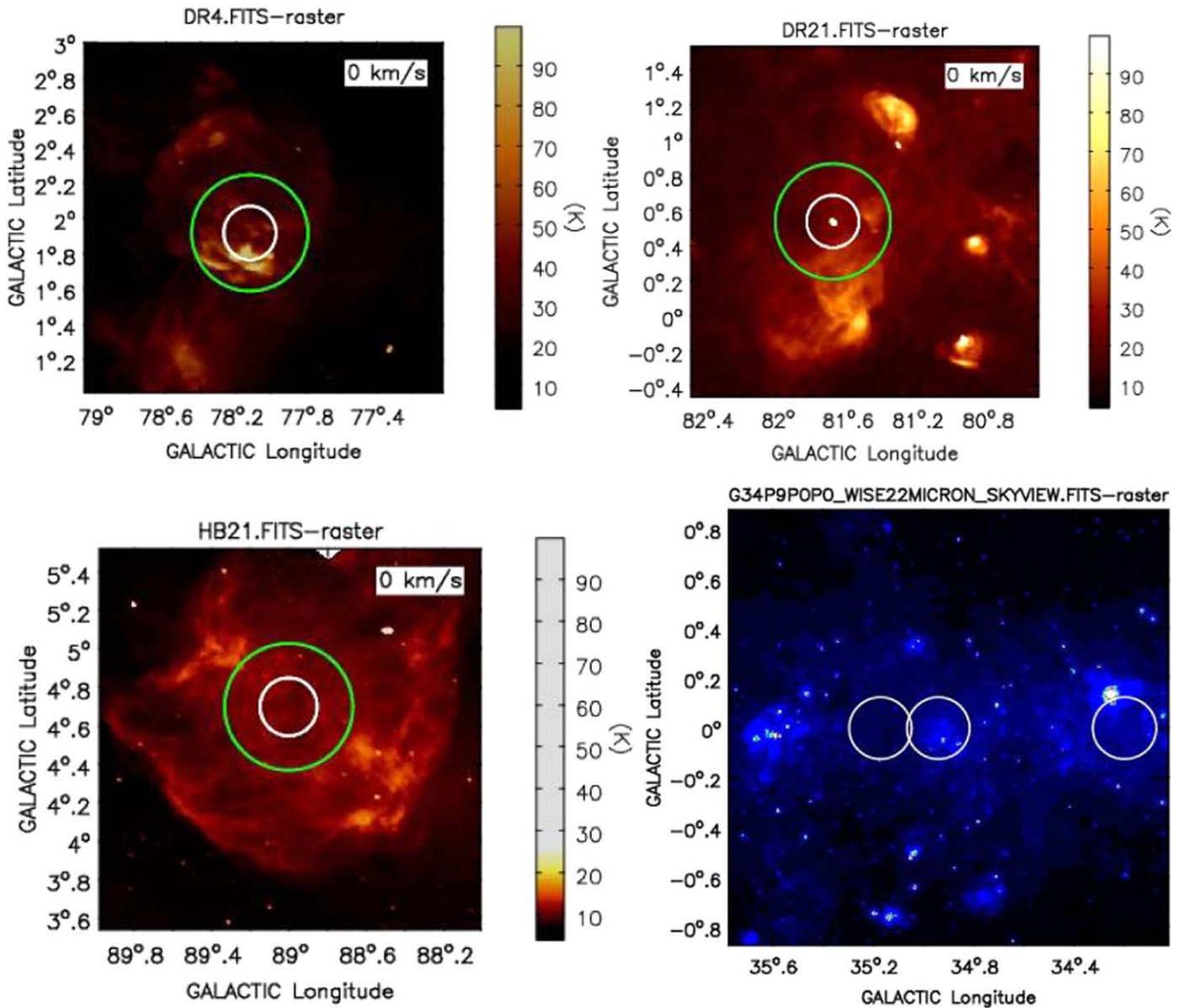
Figure 2. Top-left panel: the 1.4 GHz CGPS continuum image of DR4. Recombination line observations toward DR4 were made with the GBT. The green and white circles represent the FWHM beamwidth at 321 MHz (∼0°.66) and 750 MHz (∼0°.3), respectively. Top-right panel: same as the top-left panel but toward DR21. Bottom-left panel: same as top-left panel but toward HB21. Bottom-right panel: the three positions observed with the Arecibo telescope near 327 MHz are marked on the 22 μm Wide-field Infrared Survey Explorer image of the Galactic plane. The white circles represent the FWMH beamwidth at 327 MHz (∼0°.25).

shown in Figure 5 (top left). A Gaussian model for the spectrum extracted at 0.3° resolution is also shown in Figure 5. The line amplitudes, central velocities, and FWHM line widths of the model components are given in Table 3. The central velocity of the HISA feature agrees to within 2σ of the central velocity of the 750 and 321 MHz CRRLs (see Figure 5, bottom left). Thus we conclude that the HISA- and CRRL-forming regions are colocated.

Figure 5 (top right) shows the H I line image at the peak velocity (∼ −3.2 km s^{-1}) of the absorption feature. The H I absorption is spread over the GBT beam as inferred from the lower line temperature compared to the background emission (∼99K; see Table 3). The amplitude of the absorption feature, however, shows significant variation (see Figure 5, top right), which could be due to a combination of variation in background continuum temperature, amplitude of the background H I emission, and the properties of the cold gas. We

conclude that the self-absorption feature is extended over the GBT beam with which the RRL observations were made.

We follow the method outlined by Dénes et al. (2018) to constrain the properties of the cold gas responsible for the HISA. The spin temperature, T_s, of the absorbing gas can be written as (Equation (4) in Dénes et al. 2018)

$$T_s = \frac{T_{\mathrm{ON}} - T_{\mathrm{OFF}}}{1 - e^{-\tau_{\mathrm{HISA}}}} + T_c + p\, T_{\mathrm{OFF}} \qquad (1)$$

where T_{ON} and T_{OFF} are, respectively, the observed H I spectrum and that in the absence of absorption (both obtained after continuum subtraction), τ_{HISA} is the line optical depth of the absorbing gas, T_c is the brightness temperature of the continuum emission behind the absorbing gas, and p is a parameter used to express the background H I emission as a fraction of T_{OFF}. Equation 1 assumes the line optical depths of
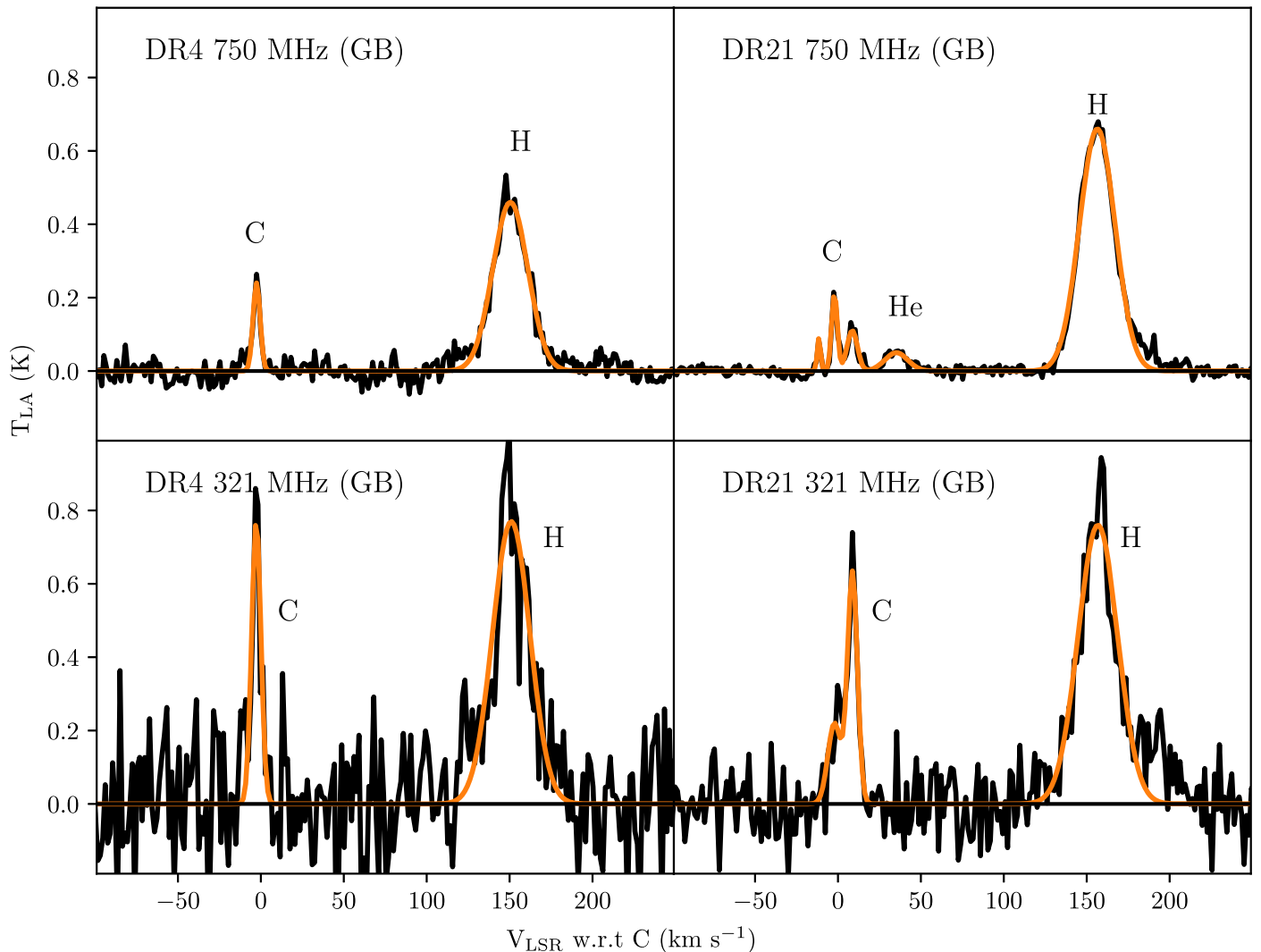
Figure 3. Radio recombination line spectra along with Gaussian line models toward DR4 and DR21. The data toward the two sources were obtained using the GBT at 750 and 321 MHz.

the background and foreground gases producing the H I emission are negligible. The peak optical depth of the absorbing gas is given by

$$\tau_{\text{HISA,peak}} = 5.2 \times 10^{-19} \frac{N_{\text{HI}}}{T_s \, \Delta V} \qquad (2)$$

where N_{HI} is the H I column density of the absorbing gas in units of cm^{-2} and ΔV is the FWHM line width of the H I absorption in km s^{-1}.

Gaussian line modeling of the H I spectrum averaged over a 0°.3 beam was used to get T_{ON} and T_{OFF}, as well as ΔV of the absorption component (see Table 3), and T_c is obtained from the CGPS continuum image. Figure 5 (bottom right) shows the cold gas T_s and N_{HI} that are consistent with the observed HISA for $p = 0.8$ and 0.9; we assume a large fraction of T_{OFF} is located behind the absorbing gas. The continuum emission varies within the GBT beam, so we examine the spectra against different bright continuum background sources. We also assume that the physical properties of the cold H I are similar over the beam area. With these assumptions, we estimate that the physical parameters of the cold H I gas are $T_s < 55K$ and $N_{\text{HI}} < 7 \times 10^{20}$ cm^{-2} for $p = 0.9$.

4.1.2. Gas Properties Derived Using CRRL Data

The carbon line intensity and line width at a given frequency depend on the electron temperature (T_e), electron density (n_e), LOS path length, background radiation field, and the non-LTE parameters characterizing the atomic level population (e.g., Payne et al. 1994; Roshi & Kantharia 2011; Salas et al. 2017; Salgado et al. 2017b). Thus observations of multiple CRRL transitions are required to constrain the physical properties of the gas (Oonk et al. 2017). We combine our data set with the LOFAR CRRL observations toward DR4 at 150 MHz ($n = 350$) to estimate the physical properties. The angular resolution of LOFAR observations is $\sim 10'$ at this frequency. The details of the LOFAR observations will be described elsewhere (J. B. R. Oonk et al. 2021, in preparation). All three CRRLs observed toward DR4 are shown in Figure 6. The LOFAR spectra are obtained by extracting the average line temperature within an aperture equal to the two GBT beam sizes.

The width of the CRRL is affected by Doppler (thermal and nonthermal), pressure, and radiation broadening. The latter two strongly depend on the quantum number, electron density, and background radiation field (e.g., Payne et al. 1994;
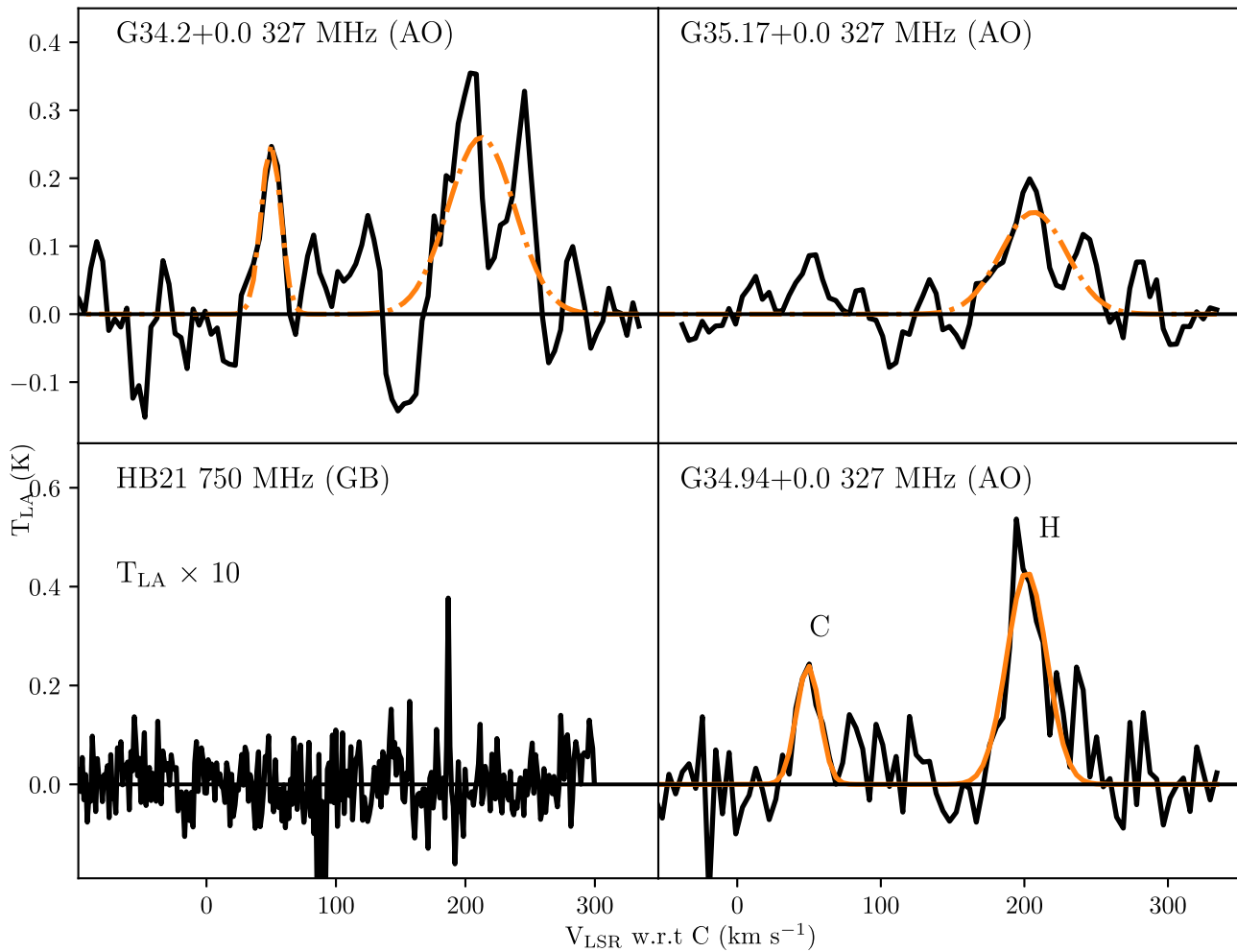
Figure 4. Radio recombination line spectra toward G34.2 + 0.0, G35.17 + 0.0, G34.94 + 0.0, and HB21. The data toward the first three sources were obtained with the Arecibo Telescope at 327 MHz, and those toward HB21 were obtained with the GBT at 750 MHz. The Gaussian line models (orange solid and dashed–dotted curves; the latter indicates tentative detection) are over-plotted in those spectra where lines were detected.

Salas et al. 2017). The line profile due to Doppler broadening is a Gaussian function while the profiles due to pressure and radiation broadening are Lorentzian functions. The net line profile is a Voigt profile that results from the convolution of the Gaussian and Lorentzian profiles. The FWHM line width of the Voigt profile can be expressed as

$$\Delta V \approx 0.53 \Delta V_L + \sqrt{0.22 \Delta V_L^2 + \Delta V_D^2}, \qquad (3)$$

where ΔV_D and ΔV_L are the FWHM widths of the Gaussian and Lorentzian profiles, respectively. For a given T_e and background temperature T_c, we can compute the Voigt line width ΔV as a function of frequency and determine the n_e values that are consistent with the observed data. An implicit assumption in the modeling is that a homogeneous gas with one LSR velocity component is present along the sight line. If multiple line-forming regions of similar temperature but with different LSR velocities are present, then the derived electron density should be considered as an upper limit.

Careful estimation of the line width is thus crucial to constrain the physical parameters of the line-forming region. We model the line profiles at 750 and 321 MHz with Gaussian functions, as the "Lorentzian wings" are not apparent at these frequencies. A Voigt profile is necessary to model the 150 MHz

line feature. The spectral baseline removal of the 150 MHz spectrum is critical, as it affects the measured line width. Line parameters obtained after removing a third-order polynomial from the 150 MHz spectrum and those obtained without baseline removal are given in Table 2 (see Figure 6). The line parameters listed are the amplitude, central velocity, and the FWHM Lorentzian line width. We fix the value of ΔV_D as the width of the line at 750 MHz for the Voigt profile modeling, as the total contribution from radiation and pressure broadening at this frequency is only about 0.5% of the observed line width.

The electron densities obtained from the line width modeling are in the range 1.4–6.5 cm^{-3} for the assumed electron temperature range 200–20 K. The temperature range is chosen based on the modeling results of low-frequency CRRL observations toward other directions in the Galaxy (e.g., Kantharia & Anantharamaiah 2001). The models used for background temperature are given in Table 4. The values for T_c at 1430.4 MHz and their uncertainties are obtained from the CGPS image, and the spectral index values, α, are taken from Ladouceur & Pineault (2008). The range of the derived physical parameters includes uncertainties in the line widths and the variation in T_c at different frequencies. We have included the range of line widths derived from the 150 MHz spectra with and without baseline removal in the uncertainty of the line width. Two example plots of the expected line widths
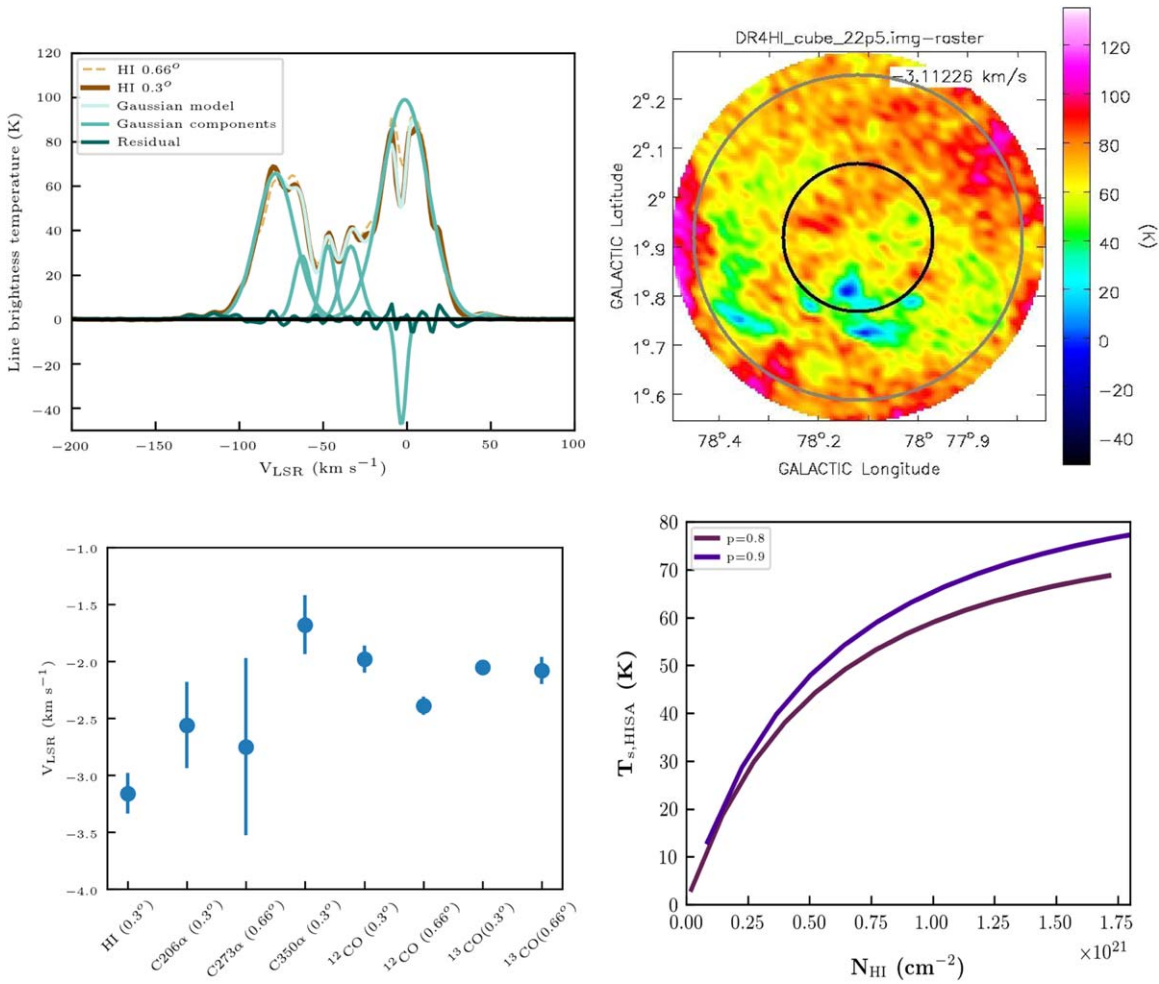
Figure 5. DR4 compilation. Top-left panel: H I 21 cm spectra averaged over 0°.66 and 0°.3 beams. Gaussian components of the 0°.3 averaged H I spectrum are shown along with the net Gaussian line model and residual obtained after removing the line model from the observed spectrum. Top-right panel: CGPS 21 cm image obtained from the spectral channel data near the peak of the HISA velocity of −3.2 km s^{-1}. The angular resolution of the image is ∼2′.5. The gray and black circles indicate the GBT beam sizes at 321 MHz and 750 MHz, respectively. The peak amplitude of the background emission near −3.2 km s^{-1} is 99 K. Thus, line amplitudes less than 99 K indicate H I absorption. The H I absorption is extended over the GBT beam, but the absorption amplitude changes within the beam area. This change could be due to a combination of variations in physical properties and background continuum. Bottom-left panel: LSR velocities of H I, CRRLs, and CO lines observed toward DR4. The error bars shown are ±2σ values. Bottom-right panel: the spin temperature and H I column density of the gas responsible for self-absorption for p = 0.8 and 0.9 are shown by the solid curves (see Section 4.1.1).

as a function of quantum number along with the observed values are shown in Figure 7 (left).

The LSR velocities of the spectral lines observed toward DR4 are shown in Figure 5. While the 750 and 321 MHz CRRLs have similar central velocities (within 1σ), the central velocity of the 150 MHz CRRL is ∼0.8 km s^{-1} (4σ) lower than that of the 750 MHz line. Based on the similarity of the observed LSR velocities of the HISA feature and CRRLs at 750 and 321 MHz (see Figure 5), we assume the cold H I gas and the CRRL region coexist. We can therefore assume that the electron temperature of the CRRL-forming region is approximately equal to the kinetic temperature of the cold H I gas, which is, in turn approximately the same as its spin temperature. For a representative electron temperature $T_e = 50$ K, consistent with the upper limit obtained for T_s, the estimated electron densities are in the range 2.8–4.5 cm^{-3}. For these model parameters, the radiation broadening is in the range 3.4 to 4.1 km s^{-1}, collisional transition broadening is in the range 2.5–4.1 km s^{-1}, and collisional ionization broadening is in the range 0.6–0.9 km s^{-1} at 150 MHz. The neutral density of the region from which CRRLs originate is estimated as $\frac{n_e}{\delta A_c}$,

where $A_c = 2.9 \times 10^{-4}$ is the cosmic abundance of carbon, and $\delta = 0.48$ is the depletion factor (Jenkins 2009). The estimated neutral density is in the range 2–3.2 × 10^4 cm^{-3}.

4.1.3. Gas Properties Derived Using CO Data

The ^{12}CO (Dame et al. 2001) and ^{13}CO (Schneider et al. 2006) spectra averaged over the GBT beam are shown in Figure 7 (right). The parameters of the Gaussian line model of the components of interest here are listed in Table 3. The central velocities of the CO lines overlap with those of the CRRLs (within 2σ) but have an offset of ∼1 km s^{-1} relative to the LSR velocity of the HISA feature (see Figure 5, bottom-left panel). The ^{12}CO/^{13}CO integrated line ratios obtained from 0°.3 and 0°.66 apertures are 12 and 4, respectively. The excitation temperature for ^{12}CO, estimated from the 0.3° averaged spectrum and by assuming that the ^{12}CO line is optically thick at its peak, is ∼5 K. The low values for line ratio and excitation temperature indicate that the gas volume density is modest.

Table 3
H I, CO, and CII 158 μm Line Parameters

Amplitude (K)	Center (km s^{-1})	Width (km s^{-1})	Note
DR4 (G78.12+1.92): H I			
2.2(1.0)	48.4(2.4)	10.9(5.7)	1
99.0(1.2)	−1.2(0.1)	33.0(0.4)	$T_{\rm OFF}$
−48.0(1.5)	−3.2(0.1)	6.8(0.3)	$T_{\rm ON} - T_{\rm OFF}$
32.9(1.0)	−33.4(0.4)	13.6(1.0)	
33.3(1.4)	−47.0(0.3)	9.5(0.7)	
28.7(2.9)	−62.5(0.3)	11.3(1.0)	
65.7(0.8)	−78.3(0.5)	27.2(0.8)	
DR4 (G78.12+1.92): ^{12}CO			
2.1(0.1)	−2.0(0.1)	3.2(0.1)	1
1.3(0.1)	−2.4(0.1)	2.2(0.1)	2
DR4 (G78.12+1.92): ^{13}CO			
0.30(0.01)	−2.05(0.02)	1.86(0.04)	1
0.28(0.01)	−2.08(0.06)	2.72(0.12)	2
DR21 (G81.68+0.54):^{12}CO			
7.7(0.1)	−2.6(0.1)	5.0(0.1)	1
4.3(0.2)	8.2(0.2)	4.0(0.4)	1
3.7(0.1)	−2.3(0.1)	5.7(0.2)	2
4.9(0.1)	8.5(0.1)	3.9(0.2)	2
DR21 (G81.68+0.54):^{13}CO			
1.47(0.01)	−2.75(0.01)	3.15(0.03)	1
0.43(0.01)	8.20(0.05)	3.26(0.11)	1
0.55(0.01)	−2.38(0.03)	3.47(0.07)	2
0.63(0.01)	8.66(0.03)	3.03(0.06)	2
DR21 (G81.68+0.54):CII 158 μm			
5.84(0.04)	−2.92(0.02)	4.52(0.04)	3
HB21 (G89.00+4.70): H I			
−39.3(4.8)	−4.8(0.2)	7.0(0.7)	1
108.1(4.9)	−4.9(0.1)	22.1(0.8)	

Notes.
[1] Parameters obtained from the spectrum averaged over 0°.3.
[2] Parameters obtained from the spectrum averaged over 0°.66.
[3] Parameters from the spectrum obtained with an angular resolution of 0°.5 × 0°.2.

We use the results presented by Goldsmith et al. (2008; see also Pineda et al. 2010, their Table 1 and Figure 3) from models developed with a large velocity gradient approximation to get an estimate of the ^{12}CO column density N_{CO} and H$_2$ density. The modeling also assumes a spherical cloud with uniform kinetic temperature of 15 K, and the levels are subthermally excited (i.e., not in LTE). The model results obtained for ^{12}CO/^{13}CO abundance ratios range between 25 and 65, as this ratio is expected to vary due to chemical and/or photoeffects. Their model results provide $N_{\rm CO} \sim 10^{16}$ cm^{-2} and $n_{\rm H_2} \sim 200$ cm^{-3}. For such low-density, diffuse clouds, the H$_2$ column density per kelvin kilometer per second of ^{12}CO line emission is 2×10^{20} cm^{-2}/(K km s^{-1}; Liszt et al. 2010). Using this relationship, we find the H$_2$ column density of the CO emitting cloud toward DR4 is $\sim 10^{21}$ cm^{-2}. The range in the above derived quantities is a factor of 1.5, which is determined from

the values estimated using the line parameters from the 0.3° and 0.66° averaged spectra.

4.1.4. Physical Picture

The neutral density derived from the CRRL line width is the total hydrogen density, i.e., $n_H + 2\,n_{H_2}$, where n_H is the density of the atomic hydrogen. The total hydrogen density is in the range $2–3.2 \times 10^4$ cm^{-3}, which is more than 50 times the density ($n_{\rm H_2} \sim 200$ cm^{-3}) derived from CO data. The thermal pressure in the CRRL-forming region is $nT_e \sim 1–1.6 \times 10^6$ cm^{-3} K, where n is the estimated neutral density of the region. The thermal pressure of the CO emitting gas is ~ 3000 cm^{-3} K, at least 300 times smaller than in the CRRL-forming region. A likely scenario is that the CRRL-forming region and the cold H I gas reside in a shocked region at the boundary of, or within, the diffuse CO emitting gas. The SN that produced the remnant DR4 could be a source of the shock.

4.2. DR21

The compact H II region DR21 is part of a large complex of radio sources located in the Cygnus X region at a distance of 1.5 kpc (Rygl et al. 2012). Radio and infrared recombination line observations made toward DR21 have provided information about the ionization, the spatial and velocity structures of the ionized gas, and the properties of the interface region between the H II region and the neutral cloud in its vicinity (Pankonin et al. 1977; Vallée 1987; Roelfsema et al. 1989; Golynkin & Konovalenko 1991). Low angular resolution ($> 1'$) observations have detected a change in the central velocity of the hydrogen RRL from −5 to 6 km s^{-1} over the frequency range 8.6–1.4 GHz (Pankonin et al. 1977). This change in velocity is interpreted in terms of a simple model involving compact H II regions surrounded by an envelope of lower-density ionized gas. The H II regions are ionized by at least six OB stars as inferred from interferometric RRL observations (Roelfsema et al. 1989). Line emission from many molecular species, as well as C I and C II FIR lines, has also been observed in this direction (e.g., Jakob et al. 2007) at central velocities $\sim$−10 to +20 km s^{-1}. The bright molecular line emissions are concentrated in the velocity range $\sim$−10 to 0 km s^{-1} and $\sim$+8 to +9 km s^{-1}. These features are associated with two interacting giant molecular clouds. The negative velocity cloud is part of the DR21 complex, and the +8 to +9 km s^{-1} velocity cloud is part of the W75 complex (Dickel et al. 1978; Gottschalk et al. 2012). Cold H I gas observed as HISA features was also reported in this region near the two velocities (Gottschalk et al. 2012).

4.2.1. Carbon and Heavy-element RRLs

Figure 6 shows the CRRL spectra observed toward DR21 at 750 and 321 MHz as well as the LOFAR spectrum at 150 MHz. Three line components are detected near the expected velocity range of the carbon line in the 750 MHz spectrum. These components have LSR velocities with respect to the rest frequency of carbon of −11.5, −2.1, and 8.6 km s^{-1}. Careful examination of the 321 MHz GBT spectrum indicates that there are line emission features near velocities −2.1 and 8.6 km s^{-1}. Examination of the 150 MHz spectrum clearly shows an absorption line near −2.1 km s^{-1}, and subtracting a single component Voigt profile fit from the spectrum shows some excess absorption near 8.6 km s^{-1} (see Section 4.2.2 for further
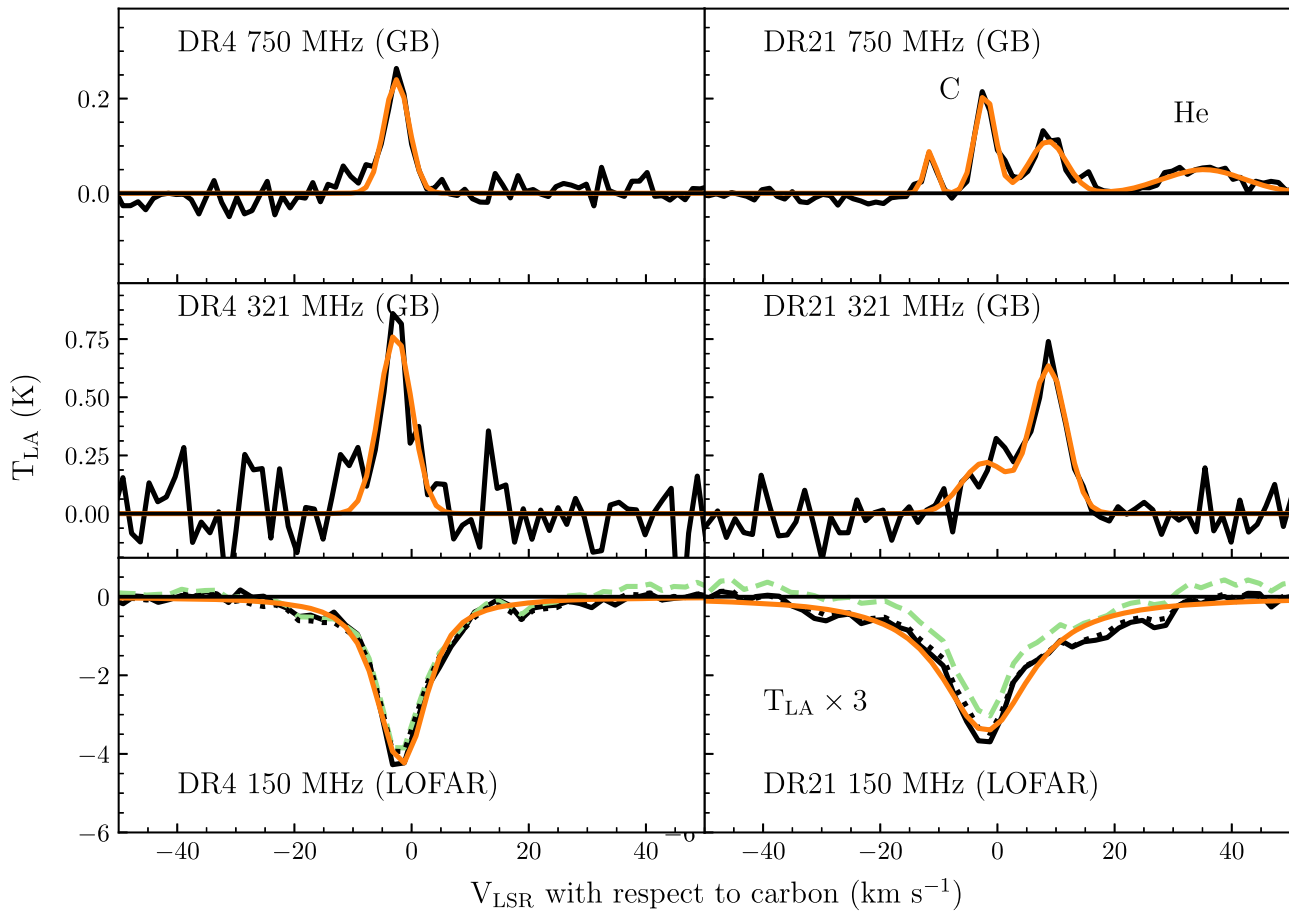
Figure 6. Carbon recombination line spectra at 750 (top), 321 (middle), and 150 (bottom) MHz toward DR4 (left) and DR21 (right). The Gaussian line models (orange curves) for the 750 and 327 MHz spectra are over-plotted. The 150 MHz spectra averaged over the 0.3° region are shown with the black solid lines in the bottom panel, and the Voigt model fit to these spectra are shown in orange solid curves. Third-order polynomials were subtracted from these spectra. The 150 MHz spectra averaged over the 0.66° region are shown by the dotted and dashed curve. No spectral baselines were subtracted from the spectra shown in dashed curve, while third-order polynomials were subtracted from the spectra shown by the dotted curve.

Table 4
Continuum Parameters Used for Modeling

Source	f_0[a] (MHz)	T_C (K)	α	Note
DR4	1420.4	46(4)	2.67 (2.63 → 2.72)	1
	1420.4	42(4)	2.67 (2.63 → 2.72)	2
DR21	150.0	2246(10)	1.94(0.01)	3
	150.0	2149(10)	2.0(0.02)	4
HB21	1420.4	10(4)	2.38	5

Notes.
[1] Continuum values obtained with 0.3° beam. The median spectral index from Ladouceur & Pineault (2008) and the interquartile range are listed.
[2] Continuum values obtained with 0.66° beam. The median spectral index from Ladouceur & Pineault (2008) and the interquartile range are listed.
[3] Continuum values obtained with 0.3° beam. The spectral index was obtained from 408 and 1420 MHz CGPS measurements.
[4] Continuum values obtained with 0.66° beam. The spectral index was obtained from 408 and 1420 MHz CGPS measurements.
[5] Continuum values obtained with 0.3° beam. The spectral index was from Kothes et al. (2006).
[a] Frequency corresponding to the listed continuum temperature T_c. The continuum temperature at a frequency f in megahertz can be obtained as $T = T_C \left(\frac{f}{f_0} \right)^{-\alpha}$.

discussion on Voigt fit to the 150 MHz spectrum). However, no emission or absorption features are seen in the 321 and 150 MHz spectra near −11.5 km s^{−1}. It is likely that this line at 750 MHz may be a transition due to a higher-mass element. For the analysis in the subsequent sections, we consider only two carbon line components at velocities −2.1 and 8.6 km s^{−1}.

We list the parameters of the previous CRRL detections (Pankonin et al. 1977; Vallée 1987; Golynkin & Konovalenko 1991) in Table 5 in order to compare with those obtained in our observations. A plot of the LSR velocities of the CRRLs, [12]CO, [13]CO, and CII 158 μm lines (see Section 4.2.4 and 4.2.6) observed in the direction of DR21 is shown in Figure 8 (left). CRRLs with positive (~8.6 km s^{−1}) LSR velocity are observed only at frequencies <1.4 GHz. The uncertainty of the central velocity of the absorption feature detected at 25 MHz (Golynkin & Konovalenko 1991) is large (about 8 km s^{−1}) compared to the errors in the central velocities of other observations; the absorption feature is likely to coexist with the negative velocity CRRL component detected in our observations (see also Golynkin & Konovalenko 1991). The mean value of the CRRL emission lines detected at frequencies >1.4 GHz is −3.0 ± 0.3 km s^{−1}, consistent (within 3σ) with the −2.1 km s^{−1} component observed in our observations, which indicates that they may be associated. CO and CII 158 μm components corresponding to both CRRL velocity features
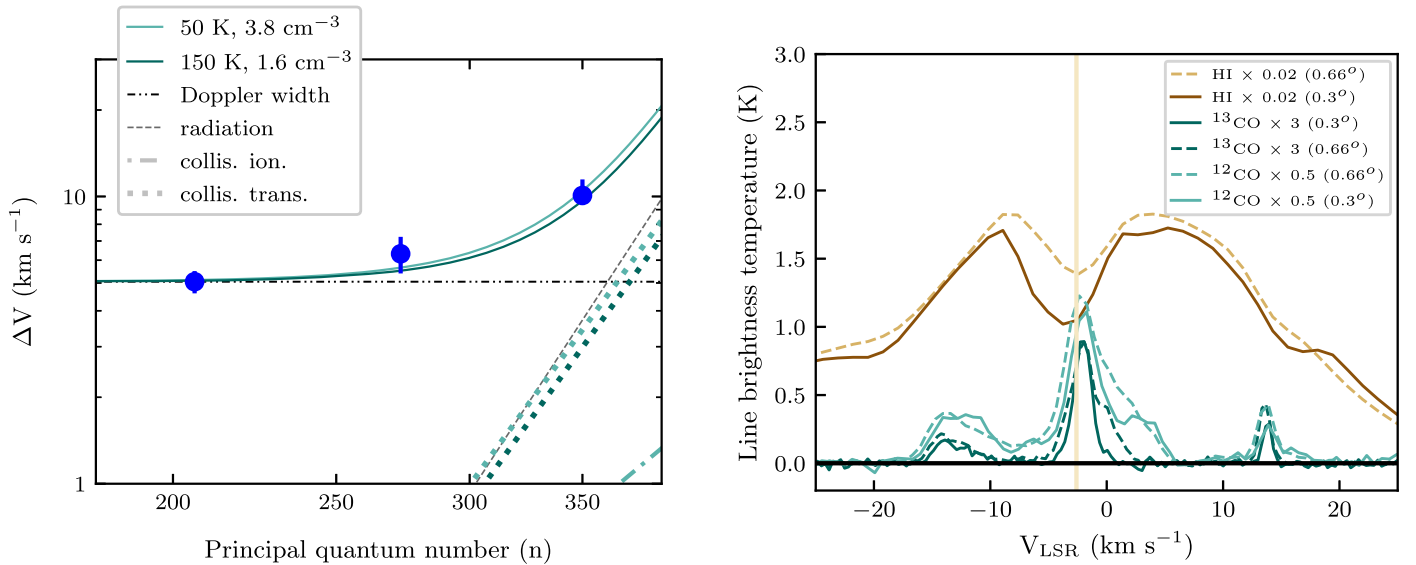
Figure 7. Left: FWHM line widths of CRRLs observed toward DR4 vs. principal quantum number. The observed points along with $\pm 1\sigma$ error bars are shown for 321 and 750 MHz observations. For 150 MHz, the effect on the line width due to baseline removal from the spectrum is also included in the error bar (see the text). The solid curves represent the expected line broadening as a function of quantum number for two different models (see Section 4.1.2), and also shown are the broadening contributions from Doppler motions (dashed–dotted–dotted line), radiation broadening with $\alpha = 2.67$ (dashed line), collisional ionizations (dotted–dashed line), and collisional transitions (dotted line) relevant for each model. Right: H I, ^{12}CO, and ^{13}CO lines toward DR4. The spectra obtained by averaging over 0.66° and 0.3° are shown as dashed and solid lines, respectively. The vertical line indicates the LSR velocity of the CRRL detected at 750 MHz.

Table 5
CRRL Parameters from Previous Observations toward DR21

Freq. (MHz)	n	T_{LA} (K)	V_{LSR} (km s^{-1})	ΔV (km s^{-1})	Note
1425	166	0.1(0.02)	–2.9(0.3)	3.2(0.6)	1
1652	158	0.1(0.02)	–3.2(0.4)	4.2(0.9)	2
3329	125	0.017(0.002)	–2.7(0.3)	4.0(0.5)	3
6482	100	0.011(0.002)	–3.0(0.2)	2.4(0.2)	4
25	640	–35(15)	0(8)	42(12)	5

Notes.
[1] Angular resolution of the observation is $8.5'$ (Pankonin et al. 1977).
[2] Angular resolution of the observation is $7.8'$ (Pankonin et al. 1977).
[3] Angular resolution of the observation is $8.2'$ (Vallée 1987).
[4] Angular resolution of the observation is $4.3'$ (Vallée 1987).
[5] Equivalent beamwidth of the observation is 1.7° (Golynkin & Konovalenko 1991).

were detected in the spectra obtained with 0.3° aperture (see Figure 8, right).

4.2.2. Constraints on the Gas Properties from CRRL Width

We follow the method described in Section 4.1.2 for modeling the CRRL line width as a function of frequency to constrain the gas properties toward DR21. The parameters of the Gaussian line models obtained from the 750 and 321 MHz spectra are given in Table 2 (see Figure 6). The signal-to-noise ratio of the –2.1 km s^{-1} component in the 321 MHz spectrum is low, which results in larger fractional errors in the estimated line parameters than were found in DR4. We attempt to fit a two-component Voigt profile to the 150 MHz spectrum, using both velocity centroids from the higher-frequency data, but the estimated error in the line parameters is comparable to the derived values. Therefore, the 150 MHz spectrum is modeled using a single component Voigt profile. The total contribution to the line width at 750 MHz due to radiation and pressure

broadening is less than 5% of the observed line width at this frequency. The estimated error of the line width at 750 MHz is 0.1 km s^{-1}, a factor of two better than the higher-frequency measurements from the literature, and the angular resolution at this frequency is comparable (within a factor of two) to the low-frequency CRRL observations. Hence for the Voigt profile fitting we used $V_D = 4.1$ km s^{-1}, the observed line width at 750 MHz. We carefully examined the spectral baseline and subtracted a third-order polynomial before modeling the line profile. The line parameters are given in Table 2. We also included line parameters that were obtained from the spectrum without any baseline removal. The line widths for the two cases differ by a factor of 1.7 (see Table 2). Thus, the effect of spectral baseline removal on the line width is substantial for the DR21 direction.

We plot the observed line width of the –2.1 km s^{-1} CRRL component as a function of quantum number in Figure 9 (left). Three example models for line width variation with quantum number are shown in the figure. The line width for the C100α line observed at an angular resolution of $4.3'$ (Vallée 1987) is not consistent with those of the lower-frequency CRRLs. This difference can be attributed to the different angular resolution between the observations, as well as changes in the gas probed as a function of frequency. As seen in Figure 9 (left), for a given $T_e = 50$ K, the electron densities required to explain the C350α (150 MHz) and the C640α (25 MHz) absorption lines (Golynkin & Konovalenko 1991) differ by a factor of 75. The situation is similar for other electron temperatures as well. Thus, at least two line-forming regions are needed to explain the observed line widths as a function of frequency. Below we attempt to separately constrain the physical parameters of these regions.

We first consider the gas responsible for the 150 MHz absorption line. Figure 9 (right) shows results from the line width modeling along with observed values at frequencies <1.4 GHz. We could not find models that are consistent with the 321 MHz observations for $T_e \gtrsim 50$ K when a 1σ range is
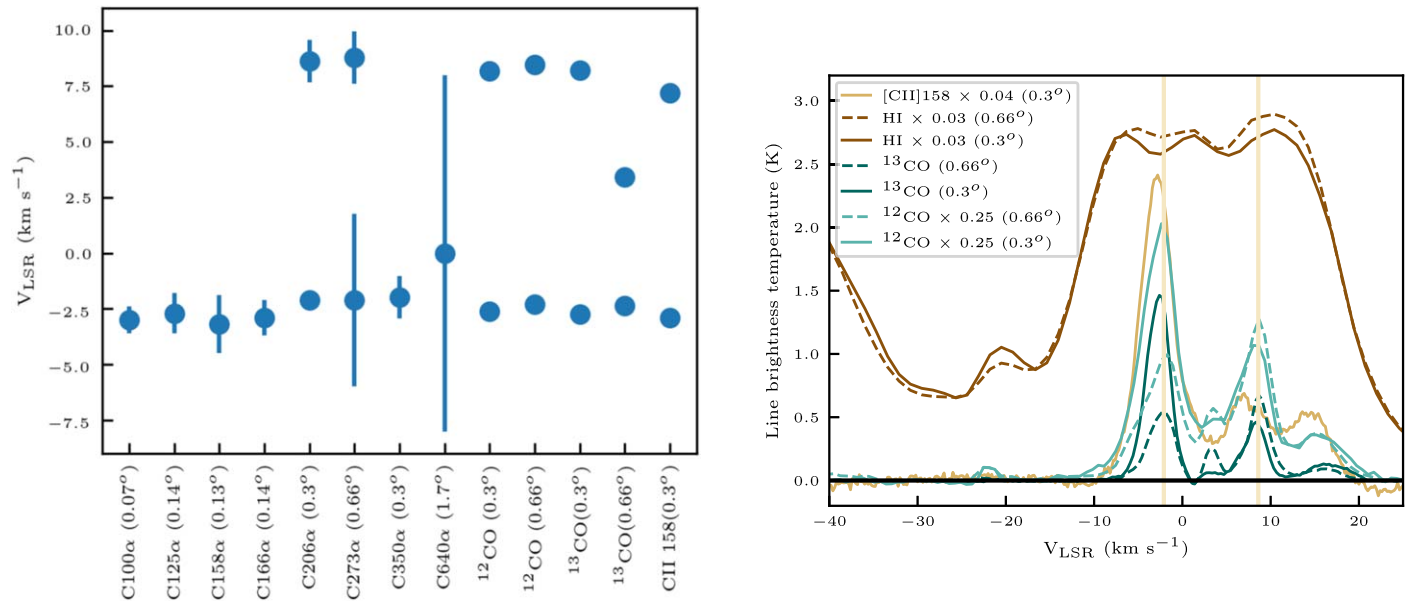
Figure 8. Left: the LSR velocities of CRRLs, ^{12}CO, ^{13}CO, and CII 158 μm lines observed toward DR21. The error bars shown are $\pm 3\sigma$ values for all data points except for the C640α line. The error bar for the C640α line is $\pm 1\sigma$. For the CO and CII 158 μm lines, the error bars are within the size of the marker. Right: H I, ^{12}CO, ^{13}CO, and CII 158 μm spectra toward DR21. The angular resolution and scaling applied to the spectra are indicated in the legend. The vertical lines indicate the LSR velocities (-2.1 and 8.6 km s^{-1}) of the CRRLs detected at 750 MHz.

considered for the observed values. An example model result that is consistent with all of the observed line widths between 750 and 150 MHz requires $T_e = 20$ K and $n_e = 24$ cm^{-3} (see Figure 9, right). Since the signal-to-noise ratio of the -2.1 km s^{-1} component at 321 MHz (C273α) is low, we include here models that are consistent only with the 750 and 150 MHz observations. The estimated electron densities from the line width modeling are in the range 3.5–24 cm^{-3} for assumed electron temperatures in the range 200–20 K. The range of neutral densities corresponding to the estimated electron densities is 2.5–17.2 $\times 10^4$ cm^{-3}. We refer to this gas as the high-density CRRL-forming region.

We now consider the gas responsible for the 25 MHz CRRL absorption. The line width modeling indicates that the electron density of the gas responsible for the 25 MHz line absorption is in the range 0.008–0.3 cm^{-3} for the assumed range of electron temperatures 200–20 K. Example model curves are shown in Figure 9 (left). The estimated parameter values are consistent with the constraints on the gas properties obtained by Golynkin & Konovalenko (1991). The neutral density of the line-forming region obtained from the estimated electron densities is in the range 58–2200 cm^{-3}. We refer to this gas as the low-density CRRL-forming region.

4.2.3. Gas Properties Using CRRL Amplitude: Preliminary Results

We take representative values for the gas parameters from the range of possible values estimated in Section 4.2.2 for the dual line-forming regions: $T_e \sim 150$ K, $n_e \sim 4.5$ cm^{-3}, and LOS path length 7×10^{-3} pc for the high-density region and $T_e \sim 50$ K, $n_e \sim 0.2$ cm^{-3}, and LOS path length 0.25 pc for the low-density region (see Figure 9, left). These parameter values are not uniquely determined, which will be attempted as part of our future modeling work (see Section 5). The higher-density region could be a photodissociation region (PDR) located at the H II region–molecular cloud interface, and the lower-density region could be located in the diffuse interstellar medium along the LOS toward the source. The background continuum

temperature at 750 MHz is $\sim$99 K and so the detection of emission lines from both regions at this frequency indicates that the carbon atom level population is not in LTE. Therefore, it is essential to have the non-LTE parameters to compute the expected line intensity from the dual line-forming region model; here, we use the results from Walmsley & Watson (1982).

Our modeling shows that the observed CRRL at 150 MHz is dominated by the line absorption due to the high-density region, as its electron density is high. The CRRL from the lower-density region is in emission at 150 MHz and is amplified by stimulated emission due to the background radiation field, as its electron density is low. The relative contributions to line emission from the high- and low-density regions at 321 MHz are 10% and 90%, and at 750 MHz are 45% and 55%, respectively. The $b_n\beta_n$ values obtained from Walmsley & Watson (1982) for the low-density region parameters are -7.2, -7.4, and -2.6 for quantum numbers 206, 273, and 350, respectively. We use the $b_n\beta_n$ values -5.7, -0.6, and 6.0 for quantum numbers 206, 273, and 350, respectively, for the high-density region, which corresponds to $T_e = 100$ K and $n_e = 1$ cm^{-3} (Walmsley & Watson 1982), as departure coefficients for higher temperatures and densities are not available. We also assumed the dielectronic-subthermal case discussed by Walmsley & Watson (1982) for the modeling.

4.2.4. H I and CO Lines

The H I, ^{12}CO (Dame et al. 2001), and ^{13}CO (Schneider et al. 2010) spectra toward DR21 averaged over the 0.3^o and 0.66^o beam are shown in Figure 8 (right). The H I line shows a self-absorption feature near (within 1σ) the -2.1 km s^{-1} CRRL component, but no absorption feature is seen near the 8.6 km s^{-1} component (see Figure 8, right). The H I line structure, however, is more complex than that toward DR4 and so we could not perform a Gaussian decomposition to extract the line parameters of the absorption feature. The CRRL central
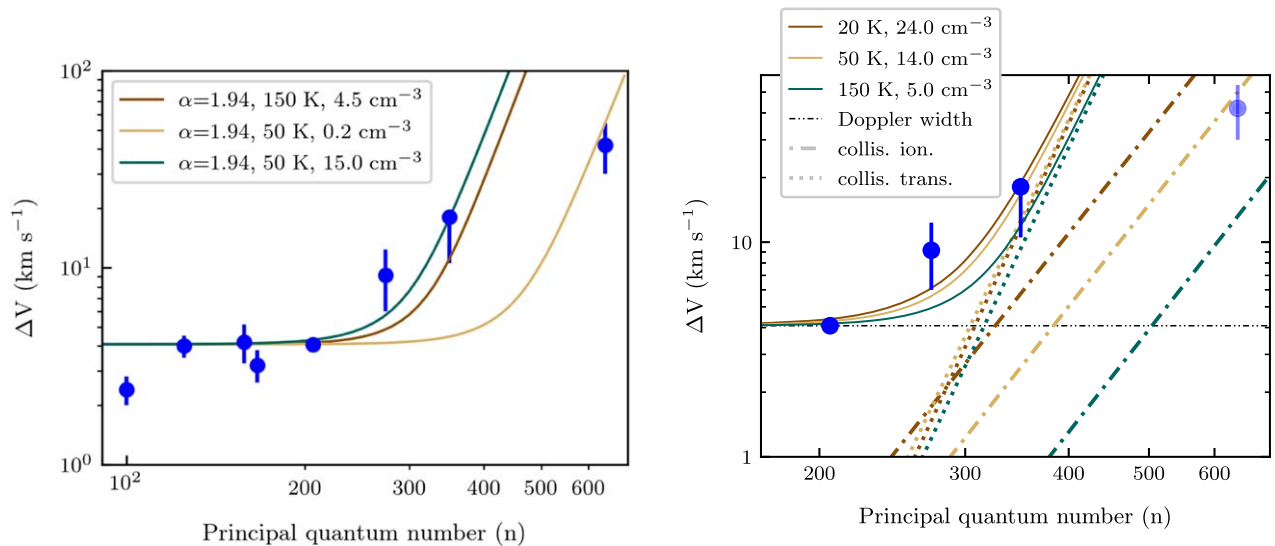
Figure 9. Left: the FWHM line widths of CRRLs observed toward DR21 vs. principal quantum number. The $\pm 1\sigma$ error bars are shown for all observed data points except for the 150 MHz line width. The error bar of the 150 MHz line width includes the range of values obtained with and without spectral baseline removal. The solid curves represent the expected line broadening as a function of quantum number for three different models. It is evident from the figure that at least two CRRL-forming regions with very different electron densities are required to explain the observed line width as a function of frequency (see Section 4.2.2). Right: same as the left panel but showing observed points at frequencies <1.4 GHz. The solid curves represent three different models for the higher-density line-forming region (see Section 4.2.2), and also shown are the broadening contributions from Doppler motions (dashed–dotted–dotted lines), collisional ionizations (dotted–dashed lines), and collisional transitions (dotted lines) relevant for each model. Radiation broadening modeled with an $\alpha = 1.94$ does not significantly contribute to line broadening in this region.

velocities are similar (within 1σ) to the two features seen in the CO spectra at -2.1 and 8.6 km s^{-1}. The CO line amplitudes in the $0.66°$ averaged spectra are lower by a factor of ~2 compared to those in the $0.3°$ averaged spectra, which indicates that the physical properties of the molecular cloud change over this angular scale. The isotopologue ratio and excitation temperature (assuming ^{12}CO is optically thick at the line center) derived from the 0.66 deg averaged spectra are 11 and 7 K, respectively. From the models of Goldsmith et al. (2008), the ^{12}CO column density and H$_2$ densities are 7×10^{16} cm^{-2} and 275 cm^{-3}, respectively, for an assumed kinetic temperature of 15 K. The estimated H$_2$ column density is 4×10^{21} cm^{-2} (Liszt et al. 2010).

4.2.5. Physical Picture

The higher-density region responsible for CRRL absorption at 150 MHz has a neutral density more than 100 times the molecular density inferred from CO line emission. The LOS extent of the molecular cloud is about 4.5 pc, at least two orders of magnitude larger than that of the dense CRRL-forming region. The enhancement in density could be due to shocks resulting from the expansion of the H II region DR21. Thus it is likely that the dense CRRL-forming region is a PDR located at the boundary of the DR21 and the associated molecular cloud. The lower-density region responsible for the CRRL absorption at 25 MHz, on the other hand, has neutral density a factor of ~5 times the CO gas density. Its LOS extent is 20 times lower than the CO cloud size. Thus the lower-density region could be residing in a denser part of the diffuse CO emitting cloud. The enhancement in density could be due to shocks resulting from the interaction of the two giant molecular clouds on this sight line.

4.2.6. CII 158 μm Emission

The CII 158 μm line was detected toward DR21 by SOFIA with an angular resolution of $0.5° \times 0.2°$ (see Figure 8 right;

Schneider et al. 2020). The line central velocity of the strongest emission is -2.92 km s^{-1} (see Table 3). This velocity is 0.8 km s^{-1} offset from the -2.1 km s^{-1} CRRL component; about eight times the uncertainty of the central velocity of the recombination line. The integrated line temperature of this component is 26.4 K km s^{-1}. We estimate the expected CII 158 μm intensity from the dual CRRL-forming region using Equation (2) of Roshi et al. (2002). The critical densities for electron, hydrogen atom, and hydrogen molecule collisions are assumed to be 10, 3000, and 6000 cm^{-3}, respectively, for electron temperatures in the range 50 to 150 K. The total hydrogen atom densities used for the calculation are estimated from the derived electron densities for the dual CRRL-forming region (see Section 4.2.3). We found that the dual line-forming region model can account for 73% of the observed CII 158 μm line intensity, with 58 % and 14% contributions from the high- and low-density CRRL-forming regions, respectively.

4.3. HB21

HB21 is an evolved, nearby SNR of age 8000–15000 yr, with an angular extent of $\sim2.5° \times 2.3°$ (Kothes et al. 2006). ^{12}CO, H I, and radio continuum observations indicate that the SNR is interacting with the interstellar material (Tatematsu et al. 1990). The 21 cm line observations show an H I shell around the SNR expanding at ~25 km s^{-1} (Assousa & Erkes 1973). A giant molecular cloud east of the remnant has been observed, and the CO emission morphology indicates that HB21 is interacting with the molecular cloud (Tatematsu et al. 1990).

4.3.1. Gas Properties Derived Using H I Data

The H I spectra averaged over the $0.3°$ and $0.66°$ regions are shown in Figure 10. The H I line near -5 km s^{-1} shows a strong emission superposed with a self-absorption feature. As in the case for DR21 and DR4, the H I profile is complex, and a
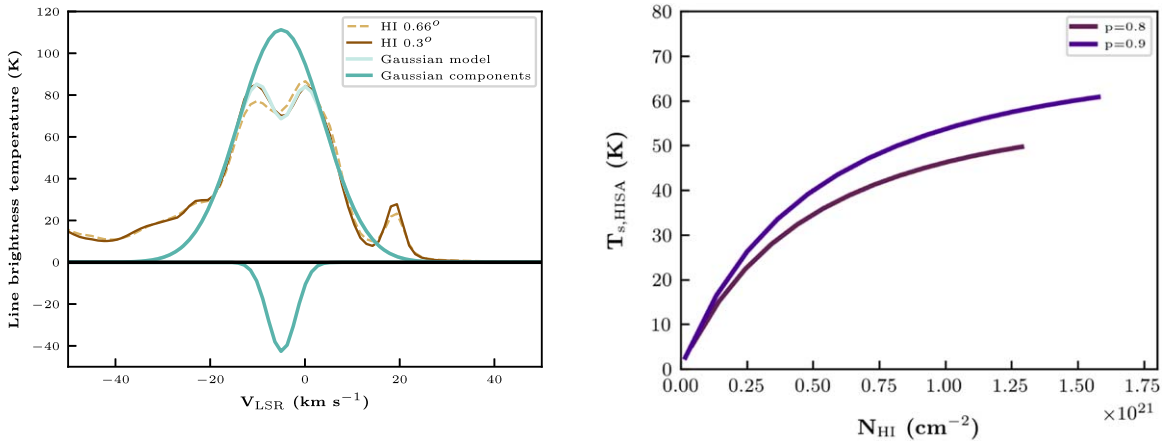
Figure 10. Left: H I 21 cm spectra toward HB21 along with Gaussian line model of the line profile. The angular resolution is indicated in the legend. Right: constraints on the physical parameters of the cold H I gas in the direction of HB21 (see Section 4.3).

unique Gaussian decomposition could not be done. We modeled the self-absorption feature using a single Gaussian emission component and an absorption component. For the line profile modeling, the velocity range was restricted to –20 to 80 km s^{-1}. The result of the Gaussian line modeling is shown in Figure 10, and the H I line parameters are given in Table 3. The properties of the cold gas responsible for HISA are constrained using the method described in Section 4.1.1. Figure 10 shows the H I spin temperatures and column densities of the cold gas that can produce the observed self-absorption feature. The H I column densities required to produce the observed absorption feature are at least 50% larger than those of the cold gas observed toward DR4.

4.3.2. Constraints from CRRL Observations

Our 750 MHz observations did not detect CRRL emission toward HB21. The upper limit on the line amplitude is 5 mK (see Table 2). Assuming an electron temperature of 50 K and taking $b_n\beta_n \sim -3.6$ (Walmsley & Watson 1982) at 750 MHz, we get an upper limit for the emission measure (EM) of 9×10^{-3} pc cm^{-6}. This EM is comparable to that of the lower-density CRRL-forming region toward DR21.

4.4. G34.20 + 0.0, G34.94 + 0.0, and G35.17 + 0.0

CRRL emission is detected toward G34.94 + 0.0 and tentatively detected toward G34.20 + 0.0 at 327 MHz (see Figure 4). Diffuse CRRL emission and absorption have been previously detected in the inner Galactic plane at frequencies above and below ∼100 MHz, respectively (Erickson et al. 1995; Kantharia & Anantharamaiah 2001; Roshi et al. 2002). The CRRLs detected with the Arecibo telescope are likely to be from diffuse C II regions similar to those observed in earlier carbon line surveys. The line width of the CRRL toward G34.94 + 0.0 is 18.5 km s^{-1}, much larger (at least a factor of four) than that seen toward DR21 and DR4 at 321 MHz, but closer to the typical line width detected in an earlier 327 MHz survey of CRRLs (Roshi et al. 2002). The larger line width could be from contributions to the observed emission from multiple line-forming regions along the LOS with different LSR velocities. Future multifrequency observations will be necessary to model the line-forming region and understand its origin.

4.5. Hydrogen and Helium RRLs

Hydrogen lines are detected toward almost all observed positions except in the direction of HB21. We estimate the EM of the H II regions responsible for the hydrogen line emission assuming LTE, electron temperature of 8000 K, and a beam filling factor of unity using the equation

$$EM = \frac{\int T_L d\nu}{1.92 \times 10^3 \, T_e^{1.5}}, \quad (4)$$

where EM is in units of pc cm^{-6}, T_e is in kelvin, and $\int T_L d\nu$ is the observed integrated line temperature in kelvin kilohertz. The EMs obtained from the 321 and 750 MHz data are 8100 and 1.1×10^4 pc cm^{-6}, respectively, toward DR4. The EMs estimated toward DR21 are 8500 and 1.5×10^4 pc cm^{-6} from the observed lines at the two frequencies. We attribute the difference in EMs obtained from the two frequencies to beam dilution effects reflecting clumpiness in the ionized gas.

The EM estimated toward G34.94 + 0.0 is 5500 pc cm^{-6}. We examined the Wide-field Infrared Survey Explorer catalog (Anderson et al. 2014) to identify H II regions in this area. The H II region G034.940 + 0.074 (Lockman 1989) is present within the Arecibo telescope beam (15′), but its LSR velocity is 45.6 km s^{-1}; no strong hydrogen RRL component at 327 MHz was detected at that velocity. A second H II region, G034.757–0.669, has LSR velocity 52.1 km s^{-1}, which agrees with the central velocity of the hydrogen RRL observed toward G34.94 + 0.0 at 327 MHz, but is at a separation of 0.7° from the sight line.

The EM estimated from the detected hydrogen line toward G34.20 + 0.0 is ∼6000 pc cm^{-6}. There are two H II regions— G034.256 + 00.136, G034.404 + 00.227—located, respectively, at angular distances of 0°.15 and 0°.3 from G34.20 + 0.0, with LSR velocities 53.1 and 60.1 km s^{-1}. The LSR velocity of G034.404 + 00.227 is within the 1σ uncertainty of the central velocity of hydrogen line detected toward G34.20 + 0.0.

Toward G35.17 + 0.0, we estimate an EM of ∼3000 pc cm^{-6}. The H II region G035.063 + 00.330 (angular distance 0.35°) has LSR velocity 57.2 km s^{-1} similar to the central velocity of the detected line toward G35.17 + 0.0.

We conclude that the hydrogen RRLs in the Galactic plane likely arise in the outer envelopes of H II regions (Anantharamaiah 1986).

A helium line is detected toward DR21 at 750 MHz. The helium to hydrogen line ratio is 0.08 (0.02). Earlier observations at frequencies of 1.4 GHz and above have found that this ratio varies from 0.03 to 0.95 within the DR21 region (Roelfsema et al. 1989). However these observations were made with an angular resolution of at least a factor of two higher than the 750 MHz observations reported here.

5. Summary and Future Work

RRLs of carbon are detected toward DR4 and DR21 at 750 and 321 MHz with the GBT. These observations are combined with 150 MHz LOFAR and other previous CRRL detections to constrain the physical properties of the line-forming regions. Modeling the line width as a function of frequency indicates that the electron density of the line-forming region toward DR4 is in the range 1.4–6.5 cm^{-3}. Similar modeling shows that a dual CRRL-forming region with electron densities 3.5–24 cm^{-3} and 0.008–0.3 cm^{-3} could plausibly explain the observed line width as a function of frequency toward DR21. The electron densities of the denser regions in both directions are at least a factor of 10 larger than those estimated for diffuse C II regions in the Galactic plane from low- (<1 GHz) frequency observations (e.g., Kantharia & Anantharamaiah 2001; Oonk et al. 2017; Salas et al. 2017). ^{12}CO and ^{13}CO emission and HISA lines at similar central velocities to the CRRLs are detected toward DR4 and DR21. The CII 158 μm lines observed toward DR21 also have central velocities similar to those of the CRRLs. The similarity of the central velocities suggests that these line-forming regions are, for the most part, associated. The inferred molecular densities from the CO data are at least two orders of magnitude smaller than that of the denser CRRL-forming regions in both directions. We suggest that the CRRLs and HISA are formed in shocked regions at the boundary of or within the cloud producing the CO emission in the direction of DR4. The shocks, which caused the enhancement of the density, could be due to SN blast waves in the case of DR4. The denser line-forming region toward DR21 could be located at the H II region–molecular cloud interface, and the density enhancement could be due to shocks caused by the expansion of the H II region. The lower-density CRRL-forming region toward DR21 has a neutral density about five times the density of the CO cloud observed in this direction. This density enhancement could be due to shocks caused by cloud–cloud collision. Our modeling shows that a significant fraction ($\sim$73%) of the observed CII 158 μm emission toward DR21 could originate from the dual CRRL-forming region.

We also detect CRRLs toward G34.20 + 0.0 (tentatively) and G34.94 + 00 near 327 MHz with the Arecibo telescope. These CRRLs could be from diffuse C II regions similar to those detected earlier in the Galactic plane (Anantharamaiah 1986).

Hydrogen lines were detected in almost all directions except toward HB21, and at all of the observed frequencies. A helium line was detected toward DR21 at 750 MHz, and the observed helium to hydrogen line ratio is 0.08 (0.02).

We plan to expand the GBT observations over a larger area in the Cygnus region to probe the spatial extent of the CRRL-forming region and to better understand its association with regions producing CO and HISA lines. We also plan to make multifrequency observations toward the Galactic plane positions where CRRLs were detected with the Arecibo telescope. Our next step in modeling the line emission is to develop a time-dependent photodissociation model that can self-consistently model the H I, CO, and CRRLs. This model will also be able to correctly calculate the level population of CRRLs at high Rydberg states. The larger data set and temporal information will help better constrain the physical properties of the absorbing clouds. The eventual goal is to derive the molecular formation rates, thus addressing the wider question of molecular cloud formation.

Facilities: Arecibo Telescope, GBT, LOFAR.

ORCID iDs

D. Anish Roshi https://orcid.org/0000-0002-1732-5990
W. M. Peters https://orcid.org/0000-0002-5187-7107
K. L. Emig https://orcid.org/0000-0001-6527-6954
P. Salas https://orcid.org/0000-0001-8271-0572
J. B. R. Oonk https://orcid.org/0000-0003-0344-2704
M. E. Lebrón https://orcid.org/0000-0001-7943-9961
J. M. Dickey https://orcid.org/0000-0002-6300-7459

References

Anantharamaiah, K. R. 1986, JApA, 7, 131
Anderson, L. D., Bania, T. M., Balser, D. S., et al. 2014, ApJS, 212, 1
Assousa, G. E., & Erkes, J. W. 1973, AJ, 78, 885

Dame, T. M., Hartmann, D., & Thaddeus, P. 2001, ApJ, 547, 792
Dénes, H., McClure-Griffiths, N. M., Dickey, J. M., Dawson, J. R., & Murray, C. E. 2018, MNRAS, 479, 1465
Dickel, J. R., Dickel, H. R., & Wilson, W. J. 1978, ApJ, 223, 840
Dobbs, C. L., Krumholz, M. R., Ballesteros-Paredes, J., et al. 2014, in Protostars and Planets VI, ed. H. Beuther et al. (Tuscon, AZ: Univ. Arizona Press), 3
Erickson, W. C., McConnell, D., & Anantharamaiah, K. R. 1995, ApJ, 454, 125
Gibson, S. J., Taylor, A. R., Higgs, L. A., & Dewdney, P. E. 2000, ApJ, 540, 851
Goldsmith, P. F., Heyer, M., Narayanan, G., et al. 2008, ApJ, 680, 428
Golynkin, A. A., & Konovalenko, A. A. 1991, SvAL, 17, 7
Gottschalk, M., Kothes, R., Matthews, H. E., Landecker, T. L., & Dent, W. R. F. 2012, A&A, 541, A79
Heeschen, D. S. 1955, ApJ, 121, 569
Jakob, H., Kramer, C., Simon, R., et al. 2007, A&A, 461, 999
Jenkins, E. B. 2009, ApJ, 700, 1299
Kalberla, P. M. W., Burton, W. B., Hartmann, D., et al. 2005, A&A, 440, 775
Kantharia, N. G., & Anantharamaiah, K. R. 2001, JApA, 22, 51
Klaassen, P. D., Plume, R., Gibson, S. J., Taylor, A. R., & Brunt, C. M. 2005, ApJ, 631, 1001
Kothes, R., Fedotov, K., Foster, T. J., & Uyanıker, B. 2006, A&A, 457, 1081
Ladouceur, Y., & Pineault, S. 2008, A&A, 490, 197
Landecker, T. L., Roger, R. S., & Higgs, L. A. 1980, A&AS, 39, 133
Li, D., & Goldsmith, P. F. 2003, ApJ, 585, 823
Liszt, H. S., Pety, J., & Lucas, R. 2010, A&A, 518, A45

Lockman, F. J. 1989, ApJS, 71, 469
Oonk, J. B. R., Alexander, E. L., Broderick, J. W., Sokolowski, M., & Wayth, R. 2019, MNRAS, 487, 4737
Oonk, J. B. R., van Weeren, R. J., Salas, P., et al. 2017, MNRAS, 465, 1066
Pankonin, V., Thomasson, P., & Barsuhn, J. 1977, A&A, 54, 335
Payne, H. E., Anantharamaiah, K. R., & Erickson, W. C. 1994, ApJ, 430, 690
Pineda, J. L., Goldsmith, P. F., Chapman, N., et al. 2010, ApJ, 721, 686
Riegel, K. W., & Crutcher, R. M. 1972, A&A, 18, 55
Roelfsema, P. R., Goss, W. M., & Geballe, T. R. 1989, A&A, 222, 247
Roshi, D. A., Balser, D. S., Bania, T. M., Goss, W. M., & De Pree, C. G. 2005, ApJ, 625, 181
Roshi, D. A., & Kantharia, N. G. 2011, MNRAS, 414, 519
Roshi, D. A., Kantharia, N. G., & Anantharamaiah, K. R. 2002, A&A, 391, 1097
Rygl, K. L. J., Brunthaler, A., Sanna, A., et al. 2012, A&A, 539, A79
Salas, P., Oonk, J. B. R., van Weeren, R. J., et al. 2017, MNRAS, 467, 2274
Salgado, F., Morabito, L. K., Oonk, J. B. R., et al. 2017a, ApJ, 837, 142
Salgado, F., Morabito, L. K., Oonk, J. B. R., et al. 2017b, ApJ, 837, 141
Schneider, N., Bontemps, S., Simon, R., et al. 2006, A&A, 458, 855
Schneider, N., Csengeri, T., Bontemps, S., et al. 2010, A&A, 520, 49
Schneider, N., Simon, R., Guevara, C., et al. 2020, PASP, 132, 19
Tatematsu, K., Fukui, Y., Landecker, T. L., & Roger, R. S. 1990, A&A, 237, 189
Taylor, A. R., Gibson, S. J., Peracaula, M., et al. 2003, AJ, 125, 3145
Vallée, J. P. 1987, Ap&SS, 129, 339
van Haarlem, M. P., Wise, M. W., Gunst, A. W., et al. 2013, A&A, 556, 2
Walmsley, C. M., & Watson, W. D. 1982, ApJ, 260, 317